Progress in Propulsion Physics **4** (2013) 373-394
DOI: 10.1051/eucass/201304373

NUMERICAL INVESTIGATION OF A HYDROGEN-FUELED SCRAMJET COMBUSTOR AT FLIGHT CONDITIONS

E. Rabadan and B. Weigand

Institute of Aerospace Thermodynamics (ITLR), University of Stuttgart
Stuttgart 70569, Germany

Numerical investigations of a hydrogen-fueled scramjet combustor at cruise flight conditions of Mach 8 at an altitude of 30 km have been performed. Two combustor configurations were investigated: a single-stage combustor with a central strut injector and a two-staged combustor combining the central strut and wall-mounted ramp injectors. These numerical simulations are aimed to study the flow structure, supersonic mixing, autoignition, and combustion for the present combustor configurations. A turbulent flow from a separate intake calculation was used as inflow condition for the combustor. A better performance for the two-staged combustor configuration was observed. The combination of the central strut injection together with the wall-ramp injection improved the turbulent mixing and, consequently, the combustion process. Inside the supersonic combustion chamber, the autoignition zone occurred downstream of the injectors, and combustion takes place accompanied by high heat release and pressure rise. As the equivalence ratio was increased, the combustion became stronger causing an upstream displacement of the shock train producing different pressure variations. For the two-staged combustor configuration, the location of the autoignition zone was found to appear further upstream compared to single-stage combustor. Mixing was improved by addition of the second-stage injection. The influence of the wall temperature was also investigated showing an effect on the combustion pressure rise and the length and location of the shock train.

1 INTRODUCTION

The scramjet engine is a promising propulsion system for hypersonic flight and a viable way to reduce costs for access to space. Scramjet powered vehicles are able to increase significantly the payload in comparison to traditional rockets. The

development of scramjet propulsion systems involves numerical investigations as well as experiments in order to achieve a better understanding of the complex flow physics occurring inside the engine. It is well known that experiments are rather expensive and demand high technical efforts, especially if real flight tests are performed. Therefore, numerical simulations are the best first approach in the design process. The Research Training Group GRK 1095 "Aerothermodynamic Design of a Scramjet Propulsion System" is focused on the scramjet technology involving highly interdisciplinary numerical and experimental studies to design and develop a scramjet demonstrator [1]. Within the framework of the Research Training Group GRK 1095, several experiments at ground conditions have been performed in the supersonic combustion facility at the Institute of Aerospace Thermodynamics (ITLR). Numerical simulations in dual mode scramjet with different injector configurations have been performed and validated against the experiments [2].

In scramjet mode, fuel has to be injected into the supersonic air stream, mixed, and then ignited, all of this within an extremely short time. In the scramjet, the combustion highly depends on the turbulent mixing, a better mixing leads to a better combustion. Usually, fuel is supplied using wall injectors, ramp, or strut injectors. These devices have been termed hypermixers [3]. Ramp and strut injectors have been studied previously and it was found that they improve the turbulent mixing in a rectangular divergent supersonic combustion chamber [4, 5]. For the present study, a central strut injector and wall-mounted ramp injectors are used together in order to increase turbulent mixing and, consequently, to enhance combustion. Depending on the amount of injected fuel, it is possible to switch from one combustion mode to another [6]. When the amount of the injected fuel is small, a lean combustion occurs, increasing the amount of fuel leads to strong combustion. Lean combustion is characterized by low heat release and strong combustion by a system of multiple shocks with a resulting large pressure rise. However, too much fuel can lead to thermal choking caused by the large heat released in the combustion chamber. Experimental research in the ground-based test facility at ITLR using a two-staged combustor have shown the capacity of the second-staged injection to extend the amount of injected fuel, thus enhancing the combustion and avoiding the risk of thermal choking [7]. Within the framework of the GRK 1095/2, a new scramjet demonstrator for flight configuration with a cruise Mach number of Ma = 8 at an altitude of 30 km is proposed [8]. The scramjet demonstrator consists of an intake with a compression ramp and sidewalls, followed by an isolator, a combustor, and a nozzle. For the present design, a study of the flow phenomena like shock wave boundary layer interactions, separations, mixing, transition mode, and turbulence–chemistry interactions is necessary in order to understand the complex physics occurring at specific flight condition. Therefore, this research is focused on the study of the supersonic combustor with single- and two-staged injection.

2 SUPERSONIC COMBUSTION CHAMBER CONFIGURATION

2.1 Single-Stage Injection

A schematic drawing of the combustion chamber is provided in Fig. 1. The total length of the combustor is 930 mm in axial direction with a maximum height of 71.42 mm at the combustor outlet. It has a constant cross-section width of 65 mm and an initial height at the entry of 41.33 mm. The combustor has a divergence angle of 1.2°. A central lobed strut injector with horizontal and vertical injection ports is used for the configuration of the single-stage injection (Fig. 2). The central injector is located 30 mm downstream from the entrance, the general dimensions are: 86 mm in length, 65 mm in width, and 7 mm in height. The strut injector has 7 horizontal and 6 vertical injection ports. The area of each horizontal and vertical port is 5.25 mm^2 and 1.20 mm^2, respectively. Hydrogen is injected parallel to the flow and mixed downstream by means of strong streamwise vorticity produced by the strut geometry. As explained in [5], at the leading edge of the injector, a shock wave is formed followed by two expansion fans at the middle of the strut. A difference in static pressure between the expansion fans produce a secondary flow. The same process but in opposite

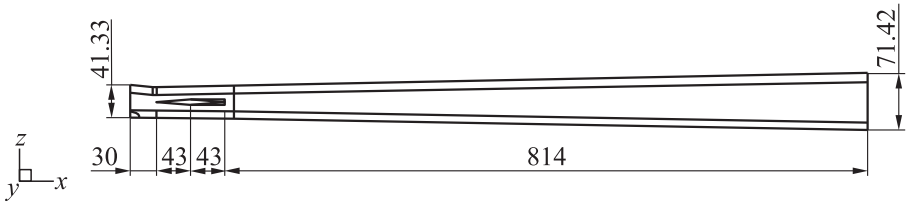

Figure 1 Schematic representation of the single-stage supersonic combustion chamber. Dimensions are in millimeters

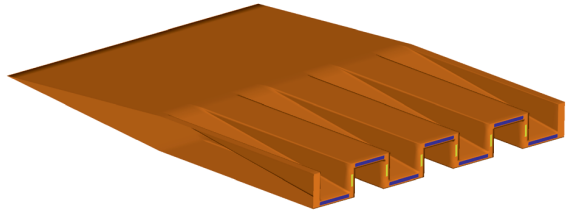

Figure 2 Central lobed strut injector. Horizontal injection ports are colored in blue and vertical ports in yellow.

direction takes place at the bottom side of the injector with the same direction of rotation. The flows in cross-stream direction from the top and bottom sides join at the trailing edge creating the vortices. This type of hypermixer has shown enhancement of the hydrogen–air mixing process in comparison with the traditional ramp injectors.

2.2 Two-Staged Injection

The two-staged supersonic injection configuration combines a central injection (lobed strut injector) together with wall-mounted ramp injection. Figure 3 shows a sketch of the two-staged injection combustor. The geometry of the combustor remains constant for the single and two-staged configuration. The position of the central strut injector is the same for all cases ($x = 30$ mm). For the second injection stage (wall ramps), hydrogen is injected parallel to the main stream at the axial location $x = 190$ mm which corresponds to the trailing edge of the ramp injector. The leading edge of the wall-ramp injector is placed at $x = 168.50$ mm. The general dimensions of the wall-ramp injectors are: height 4 mm, width 10 mm, total length 21.50 mm, and area of hydrogen injection 7 mm^2 with an injection angle of 15°. This geometrical features correspond to the injectors used in the experimental campaign conducted at ITLR for the ground testing configuration [7]. To increase the mixing in the second stage, the wall ramps are separated in lateral direction in such a way that it is intended to reproduce the same effect of the central strut injector creating vortices as the flow passes through the ramps. A total of 6 wall-mounted ramp injectors are placed in the combustor, three ramp injectors at the top wall and three at the bottom wall.

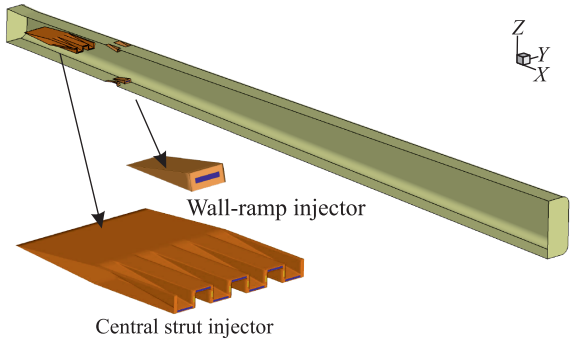

Figure 3 Geometry of the two-staged injection configuration. A cut through the symmetry plane shows the location of the central strut injector and the wall-mounted ramp injectors.

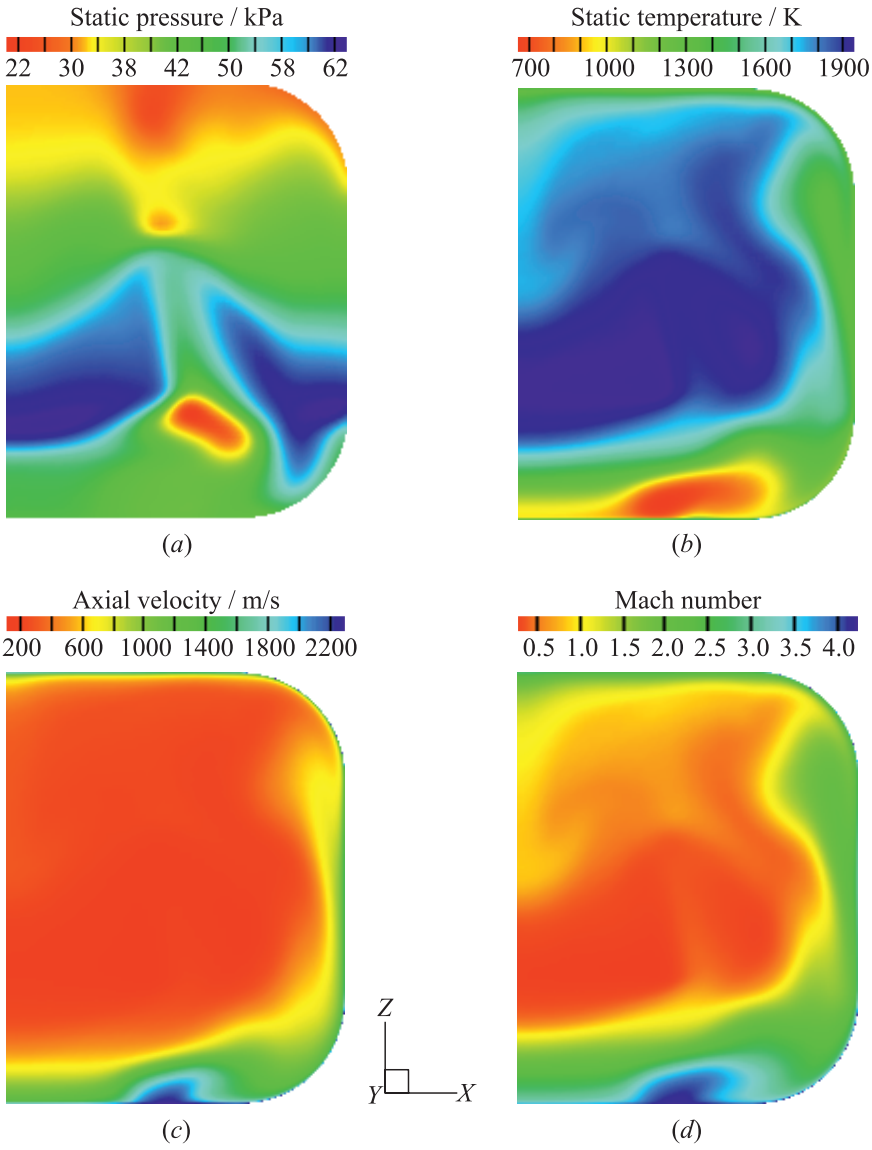

Figure 4 Inflow profiles within the combustion chamber, courtesy of T. Nguyen [8]: (*a*) static pressure; (*b*) static temperature; (*c*) axial velocity; and (*d*) Mach number.

3 NUMERICAL MODELING

3.1 Inflow Conditions

The inflow conditions used for the present investigations correspond to the flight condition design at a cruise Mach number of Ma = 8 at an altitude of h = 30 km. The flow conditions at the entry of the combustor were provided by Nguyen [8]. The inflow profile used at the entry of the combustor comes from the intake with compression ramp and sidewalls. The actual intake configuration increases the capture of air mass flow and compression efficiency but, on the other hand, provides a nonuniform flow field at the interface of the combustion chamber. To take average values at the entry of the combustor is not a realistic assumption due to the nonuniformity of the flow field. Thus, to obtain useful results, the full three-dimensional (3D) cross-section flow profile at the intake–combustor interface was used. The inflow profile contains all necessary variables to precisely describe the flow field coming from the inlet towards the combustor preserving all features of the already developed flow field like shock waves, turbulent boundary layer, separation regions, kinetic energy, etc. Figure 4 shows the distribution of Mach number, static temperature, axial velocity, and static pressure at the entry of the combustor. Table 1 shows the mass weighted average values of these variables. For all simulations, hydrogen was injected at a static temperature of T_{H_2} = 300 K, in the supersonic regime at Ma = 2 and 1.5 for the horizontal and vertical injection jets, respectively. The static pressure of the hydrogen was varied to adjust the hydrogen mass flow in order to satisfy the desired equivalence ratio.

Table 1 Mass weighted average values of the thermodynamic properties at the inlet of the combustor and hydrogen jet inflow conditions

Location	p, kPa	T, K	u, m/s	Ma
Combustor inlet	42.95	879.37	2033.31	3.57
Hydrogen horizontal jet	$f(\phi)$	300	2632.17	2
Hydrogen vertical jet	$f(\phi)$	300	1974.12	1.5
Hydrogen wall-ramp jet	$f(\phi)$	300	1974.12	1.5

3.2 Numerical Setup

Three-dimensional structured grids were used to study the flow phenomena in the combustor. To reduce the computational domain, symmetry was used to simulate half of the combustor. For the single-stage combustor, grid convergence studies were performed using a nominal grid with $1.88 \cdot 10^6$ cells, a medium grid with $2.89 \cdot 10^6$ cells, and a finer grid with $3.99 \cdot 10^6$ cells. No significant differences

were observed between the nominal and the medium grid. For the nominal and finer grid, small discrepancies specially in the wall pressure distribution due to higher resolution at the walls were observed. However, all simulations were performed with the nominal grid since no considerable discrepancy was found. For the two-staged injection, two structured grids were investigated: a nominal grid with $3.28 \cdot 10^6$ cells and a finer grid with $4.07 \cdot 10^6$ cells. Similarly to single-stage injection, no considerable variation between the nominal and finer grid was observed; therefore, the nominal grid was used for the computations.

The numerical investigations were performed using the commercial code CFD++ version 10.1 [9] which has previously been validated in [7, 10] for supersonic combustion cases. A 3D axisymmetric model with hexahedral elements and cell centered variable storage was used. Fluxes were computed to second-order accuracy. Steady-state solution was performed for all numerical computations. The equation set used were Reynolds-averaged Navier–Stokes (RANS). The governing equations for mass, momentum energy, and species, describing convection, diffusion, and reactions were solved point-implicit. Local time stepping with constant Courant–Friedrichs–Lewy number of CFL = 20 was used. To identify a converged steady-state solution, attention was paid to the residuals of the Navier–Stokes equations, turbulent kinetic energy, turbulence inverse timescale, and concentration of species. For all converged solutions residuals have dropped between 3 and 4 orders of magnitude.

Turbulence was modeled by the two-equation Shear Stress Transport (SST) model using wall function. This model solves the transport equation for turbulent kinetic energy k and for turbulence inverse time scale ω. The latter is modified such that ω in the near-wall regions is blended with ϵ (the turbulence dissipation rate) further away from walls and in the wake region [9]. For initialization, the turbulence level of all incoming flows was set to 2% and the ratio of turbulent to laminar viscosity was predefine $\mu_T/\mu_L = 50$. A constant turbulent Schmidt number $\mathrm{Sc}_t = 0.80$ and laminar/turbulent Pr ratio of 0.8 were assumed. Combustion was modeled by the modified 9 species (N_2, O_2, H_2, H_2O, OH, O, H, HO_2, and H_2O_2), 19-step chemical kinetics model of Jachimowski [11], where nitrogen reactions and turbulence chemistry interactions were ignored [12, 13].

4 RESULTS AND DISCUSSION

4.1 Wall Pressure Distributions

For the single-stage injection configuration, series of numerical investigations varying the equivalence ratio were performed. A fuel-off case was performed in addition to be compared against the fuel-on cases. The profiles described previously (see Fig. 4) were introduced as inflow boundary conditions at the

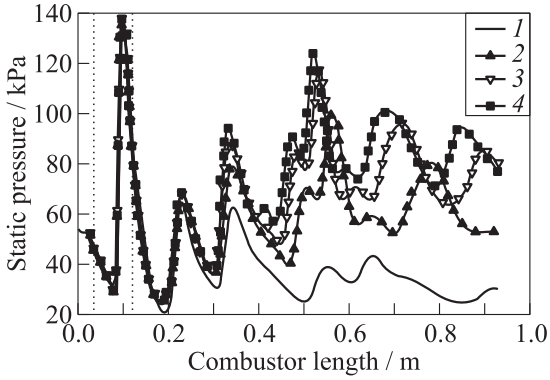

Figure 5 Computed surface pressure distribution at the top wall for different equivalence ratios: *1* — fuel-off; *2* — $\phi = 0.30$; *3* — 0.45; and *4* — $\phi = 0.55$

inlet of the combustor. Wall temperatures were set to a constant values. For the channel and injector walls, the wall temperature was set to $T_{\text{wall}} = 900$ K. The pressure of the hydrogen jet was varied to meet the desired equivalence ratio. The equivalence ratio is defined as

$$\phi = \frac{\dot{m}_{\text{H}_2\,\text{inj}}}{\dot{m}_{\text{H}_2\,\text{st}}} = \frac{1}{2}\,\frac{M_{\text{O}_2}}{M_{\text{H}_2}}\,\frac{Y_{\text{H}_2}}{Y_{\text{O}_2}}$$

where $\dot{m}_{\text{H}_2\,\text{inj}}$ is the injected mass flow rate of hydrogen and $\dot{m}_{\text{H}_2\,\text{st}}$ is the mass flow rate of hydrogen required for stoichiometric combustion, M_{O_2} and M_{H_2} are the molecular weights of oxygen and hydrogen, respectively, and Y_{O_2} and Y_{H_2} are the mass fraction of oxygen and hydrogen, respectively. In all calculations, a supersonic outflow boundary condition for the combustor outlet was used as well as wall functions for all walls in the domain. The surface pressure distributions for the single-stage injection are plotted in Fig. 5. The pressure distribution corresponds to the top wall of the combustor in the symmetry plane. The vertical dotted lines represent the leading and trailing edge of the central strut injector. A fuel-off case is shown together with the fuel-on cases for different equivalence ratios. The fuel-off case is presented to compare the pressure rise against the reacting flow cases. Figure 5 shows how increasing the equivalence ratio results in a pressure rise. Increasing the equivalence ratio and, consequently, the injected hydrogen mass flow leads to more available fuel resulting in a stronger combustion with higher heat release. The shock structure in the combustor causes the peaks and valleys in the pressure plot. In the fuel-off case, the shock structure is caused by the geometry of the injector and the combustor. As it was stated by Carroll and Dutton [14], the general effect of the Mach number on the shock structure is that there is a tendency towards repeated shock systems as the Mach number

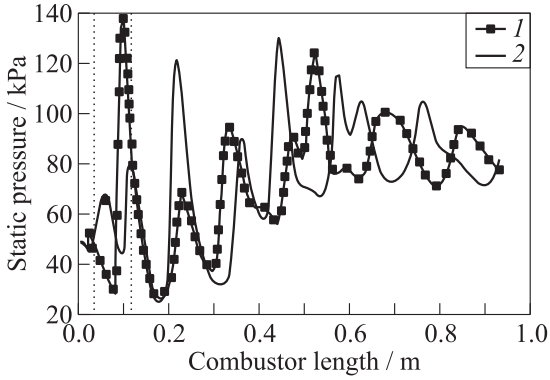

Figure 6 Computed surface pressure distribution at the top (*1*) and bottom (*2*) walls for an equivalence ratio $\phi = 0.55$

increases. The first peak in pressure rise is caused by the central injector due to the geometrical blockage of the flow. As reported by Scheuermann *et al.* [6], a disadvantage of the central injector is the geometrical blockage specially in a small-scale combustors. The intensity of the shock wave system produced by the high entry Mach number is decreased downstream of the central injector as the combustor divergence is growing.

The pressure starts to drop just before the trailing edge of the injector from 138 kPa down to 20 kPa at 188 mm from the combustor entry, that is, 72 mm away from the trailing edge of the injector. For fuel-on cases, it is possible to observe how the repeated oblique shock pattern grows in intensity as the equivalence ratio is increased, various researchers reported similar pattern for supersonic combustors [15–17]. For the fuel-on cases, the shock structure not only depends on the geometry of the combustor, but also on the heat release due to the combustion process. Increasing ϕ results in a stronger combustion and higher heat release moving the shock system in upstream direction. However, Figs. 5 and 6 show that not even for $\phi = 0.55$, the shock system moves further upstream as 330 mm. In presence of combustion, the highest pressure is observed at 520 mm (nearly the same axial location for all equivalence ratios); however, the highest pressure peak registered corresponds to the shock induced by the central injector 98 mm downstream from the combustor entry plane for both fuel-off and fuel-on cases. Increasing the equivalence ratio up to $\phi = 0.55$ does not influence the shock wave pattern for the first 250 mm in the flowpath of the combustor. Figure 6 shows the surface pressure distribution at the top and bottom walls of the combustor for $\phi = 0.55$. The pressure traces show the flow to be asymmetric. Different amplitudes are observed in the shock pattern for the top and bottom walls. Figure 7 shows the computed pressure gradient in

Figure 7 Computed pressure gradient in the symmetry plane of the combustor ($\phi = 0.55$)

the combustor symmetry plane for an equivalence ratio $\phi = 0.55$. From here, it is possible to observe the repeated oblique shock pattern developed in the chamber in presence of combustion. Figures 6 and 7 give a visual representation of the asymmetry of the flow, where the shock deflections and pressure peaks at the top and bottom walls show some discrepancy in the axial position. The asymmetry of the flow can be attributed to the nonuniform inlet flow with a high Mach number (see Fig. 4). Wang *et al.* [18] observed similar results of asymmetric flow pattern in experiments even for uniform incoming flow at Ma = 2.13 and Carroll and Dutton [14] reported asymmetric flow for incoming flow at Ma = 2.45.

The surface pressure distribution along the combustor for different equivalence ratios using central and wall-ramp injection is plotted in Fig. 8. The surface pressure distribution corresponds to the top wall of the combustor. The dotted lines indicate the location of the leading and trailing edges of the injectors. The equivalence ratio for the central injector is kept constant to $\phi_1 = 0.30$, while the equivalence ratio for the wall-ramp injectors is varied from $\phi_2 = 0.25$ to 0.55. It has been observed that combining a central injection together with wall-ramp injection results in an enhancement of the combustion.

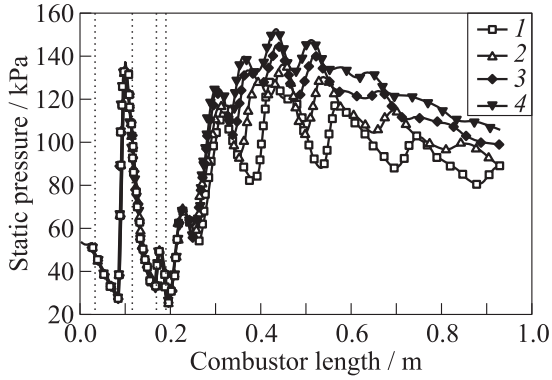

Figure 8 Computed surface pressure distribution at the top wall for different total equivalence ratios. In the two-staged injection, ϕ_1 and ϕ_2 indicate the central injection and wall-ramp injection, respectively; $\phi_1 = 0.30$: *1* — $\phi_2 = 0.25$; *2* — 0.35; *3* — 0.45; and *4* — $\phi_2 = 0.55$

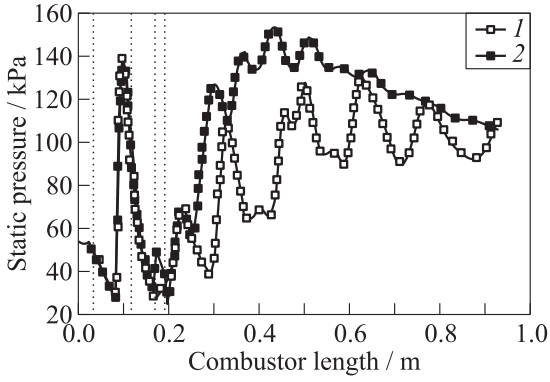

Figure 9 Comparison of the computed surface pressure distribution at the top wall between the single- (*1* — $\phi = 0.85$) and two-staged injection at the same equivalence ratio (*2* — $\phi_1 = 0.30$, $\phi_2 = 0.55$)

Figure 10 Computed pressure gradient in the symmetry plane of the combustor ($\phi_1 = 0.30$ and $\phi_2 = 0.25$)

Figure 9 shows a comparison between single- and two-staged combustors. For both cases, the total equivalence ratio is $\phi_{\text{tot}} = 0.85$. The highest pressure peaks correspond to the configuration with two-stage injection. The shock train in front of the second injection remains unaltered for both cases. After the wall-ramp injector, the difference in pressure peaks becomes clear, more heat is released due to the enhancement of the combustion, modifying the intensity and location of the shock system. For the same operation conditions, it was found that using a second-stage injection, the combustion takes place approximately 120 mm upstream in comparison to the single-stage injection.

Figure 10 shows the computed pressure gradient to visualize the shock system developed in the combustor using central injection together with wall-ramp injection ($\phi_1 = 0.30$ and $\phi_2 = 0.25$). Besides the asymmetry of the flow pattern previously described, the altered shock structure is also visible (compared with Fig. 7). At the base of a ramp, a new oblique shock arises producing counter-rotating vortices due to the difference in pressure between the compressed air above the ramp and the lower pressure in the ramp sidewalls. The new formed oblique shocks over the top and bottom ramps are projected downstream increasing the thermodynamic properties of the surrounding flow thus, improving the conditions for autoignition of the air–fuel mixing.

The description of the flow field in terms of static temperature, Mach number, H_2 and OH species for the single-stage combustor is plotted in Figs. 11–14. A comparison between the two equivalence ratios $\phi = 0.30$ and 0.55 is made. Higher amount of injected hydrogen results in a stronger combustion and higher heat released. For $\phi = 0.30$, the highest temperature is kept in the central axis of the channel, rather than for $\phi = 0.55$ where the temperature covers more of the cross section along the combustor. The maximum temperature in the core flow exceeds 2500 K. In the near field of the strut trailing edge, no increase

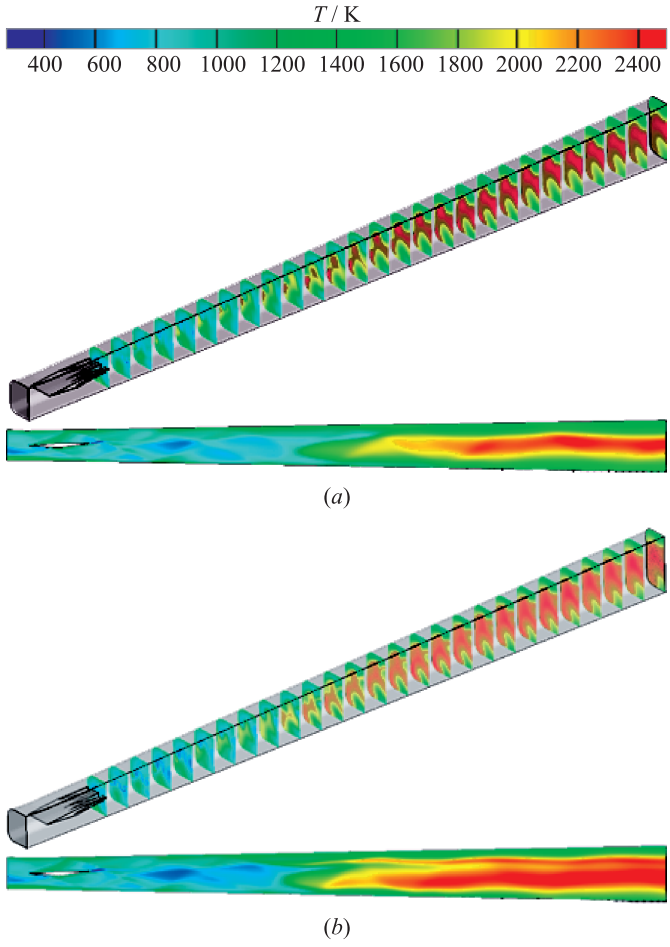

Figure 11 Computed static temperature distribution. The 3D model represents half of the combustor. The two-dimensional plot shows a cut at the symmetry plane: (*a*) $\phi = 0.30$ and (*b*) $\phi = 0.55$.

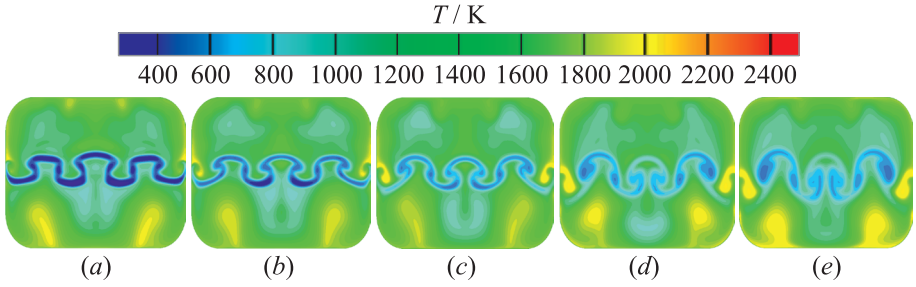

Figure 12 Computed temperature contours describing the hydrogen temperature (dark blue) $T_{H_2} = 300$ K ($\phi = 0.55$). The intensity of the hydrogen temperature contours decreases downstream as the hydrogen is mixed in the surrounding flow. The frames represent the full cross-section area of the combustor channel: (a) $x = 135$ mm; (b) 148; (c) 160; (d) 179; and (e) $x = 192$ mm.

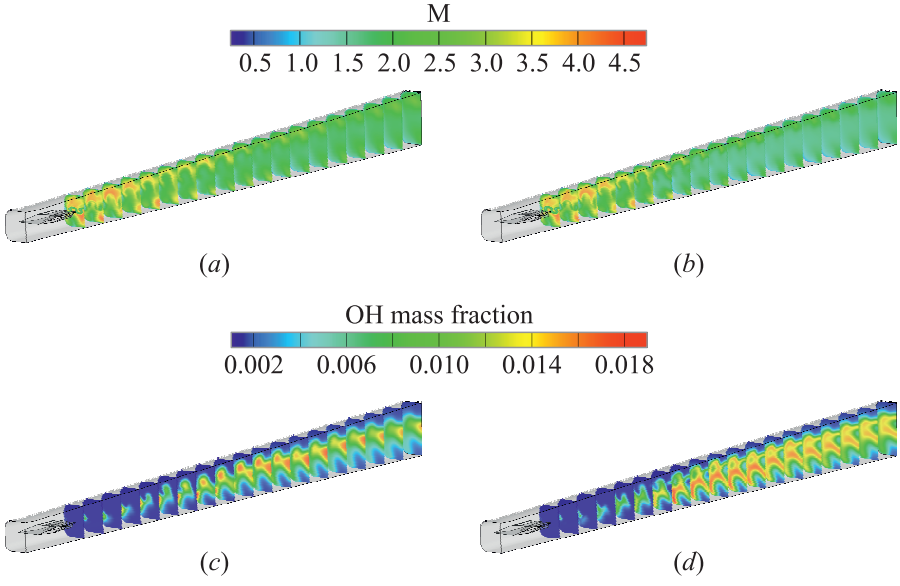

Figure 13 Computed flow field variables for half of the combustor geometry: (a) Mach number distribution, and (b) OH mass fraction distribution. Left column refers to $\phi = 0.30$ and right column to $\phi = 0.55$.

in temperature is observed, meaning that a lifted flame occurs (see Fig. 11). The lobed strut injector creates streamwise vortices as the flow passes through it. In the wake of the strut, injector temperature contours of 300 K can be observed (see Fig. 12). These contours correspond to the temperature at which

hydrogen is injected. Hydrogen is mixed and transported into the core of the flow due to the vorticity induced by the strut. For high equivalence ratios (i. e., $\phi = 0.55$), hydrogen is trapped into the axis of rotation of the vortices remaining unmixed for a longer distance downstream. Increasing the equivalence ratio results in a static temperature rise and, consequently, in high pressures (see Figs. 5, 8, and 11). However, for $0.30 \leq \phi \leq 0.55$, a lifted flame with no significant difference in axial location was observed.

The flow enters the combustor with supersonic speed; before the flow reaches the central injector, the velocity is decreased. This effect is caused by the shock train resulting from the geometrical blockage induced by the central injector. The Mach number rises again after the injectors maximum thickness. After the injector, the flow accelerates due to the divergence of the channel and suddenly decelerates due to the heat released by combustion. A similar pattern was observed experimentally by Vellaramkalayil *et al.* [7] and Scheuermann *et al.* [6]. Due to the small thickness of the hydrogen jet and its low momentum, velocity differences between hydrogen and air disappear quickly [5]. This is visible in the axis of the channel after the hydrogen injection, where the velocity of the hydrogen is rapidly reaching the velocity of the outer flow field. The contours downstream of the injector at the top wall show high Mach numbers, it appears that the flow at this location remains unaffected by the combustion and heat release (see Fig. 13*a*). The distribution of the OH mass fraction along the combustor length is shown in Fig. 13*b*. The OH species provides information on the structure and ignition characteristics in the combustor. In the near field, after the injection of hydrogen, the conditions for autoignition are not met; thus, the evidence of OH species concentration is not observed (lifted flame). After some distance downstream of the wake of the injector, OH becomes visible (for $\phi = 0.55$, approximately 245 mm downstream of the injector trailing edge). Further downstream, the OH contours extend over the combustor height. The highest concentration of OH appears around the central axis of the combustor indicating that combustion takes place mainly at the axis of the channel. Hydrogen profiles in the cross section of the combustor for different axial positions are shown in Fig. 14.

Figure 14 Computed hydrogen mass fraction at different axial locations ($\phi = 0.55$). Pictures represent the full cross-section area of the combustor channel: (*a*) $x = 135$ mm; (*b*) 148; (*c*) 160; (*d*) 179; and (*e*) $x = 192$ mm

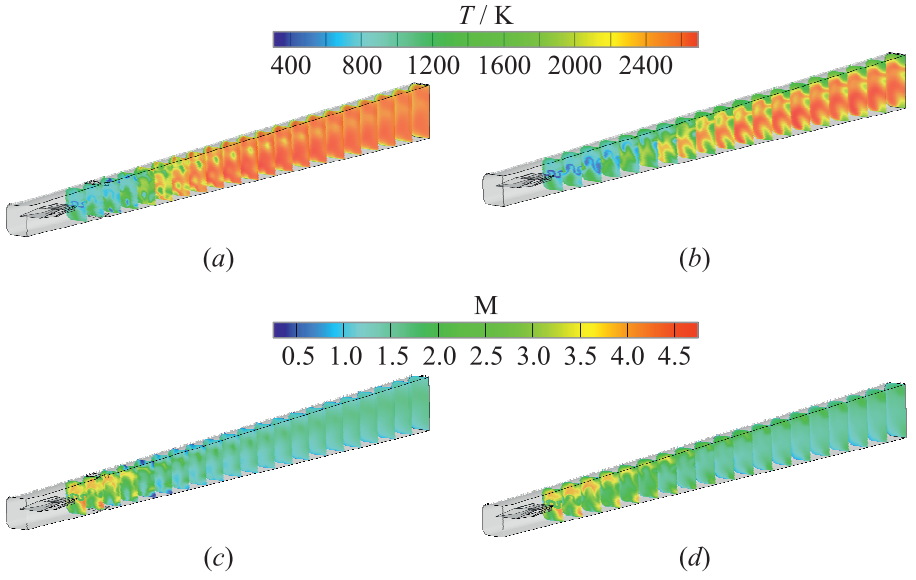

Figure 15 Computed flow field variables for half of the combustor geometry (two-staged injection configuration): (*a*) and (*b*) static temperature distribution, and (*c*) and (*d*) Mach number distribution; (*a*) and (*c*) refer to $\phi_1 = 0.30$ and $\phi_2 = 0.55$; and (*b*) and (*d*) to $\phi = 0.85$.

The flow field for the two-staged injection is presented in Fig. 15. In front of the wall-mounted ramp injectors, the flow field appears to be unaltered. From the Mach number distribution, subsonic regions produced by the wall-ramp injectors can be observed (see Fig. 15*c*). The subsonic regions appear downstream of the trailing edge with a maximum height of approximately one half of the injectors height. Some of the hydrogen is trapped in these subsonic regions but is not reacting because the thermodynamic conditions for ignition are not met (see Figs. 15*a* and 15*b*). Some distance downstream recirculation zones appear both at the top and bottom walls (see Fig. 15*c*). It is observed that increasing the mass flow of hydrogen from the ramp-injectors, the second subsonic regions move upstream. For $\phi_{\text{tot}} = 0.55$ ($\phi_1 = 0.30$ and $\phi_2 = 0.25$), the second subsonic region at the top wall appears at the global axial coordinate $x = 265$ mm rather than $x = 250$ mm for $\phi_{\text{tot}} = 0.85$ ($\phi_1 = 0.30$ and $\phi_2 = 0.55$). The maximum height of the subsonic region for $\phi_{\text{tot}} = 0.55$ ($\phi_1 = 0.30$ and $\phi_2 = 0.25$) represents approximately 15% of the total height of the channel at the local axial coordinate and 16% for $\phi_{\text{tot}} = 0.85$ ($\phi_1 = 0.30$ and $\phi_2 = 0.55$). This indicates that separation regions are produced by the geometry of the wall-ramp injectors and the amount of hydrogen injected affects mainly the axial location and not

the height of the separation region. The separation regions, both at the top and bottom walls, are vanishing further downstream after 480 mm.

The wall-mounted ramp injectors enhance the combustion process, but lead to combustion near the walls where temperatures of $T > 2200$ K (specially for $\phi_{\text{tot}} = 0.85$) are present. Comparing Figs. 15*a* and 15*b*, it is observed that for the same equivalence ratio ($\phi_{\text{tot}} = 0.85$), the temperature distribution change

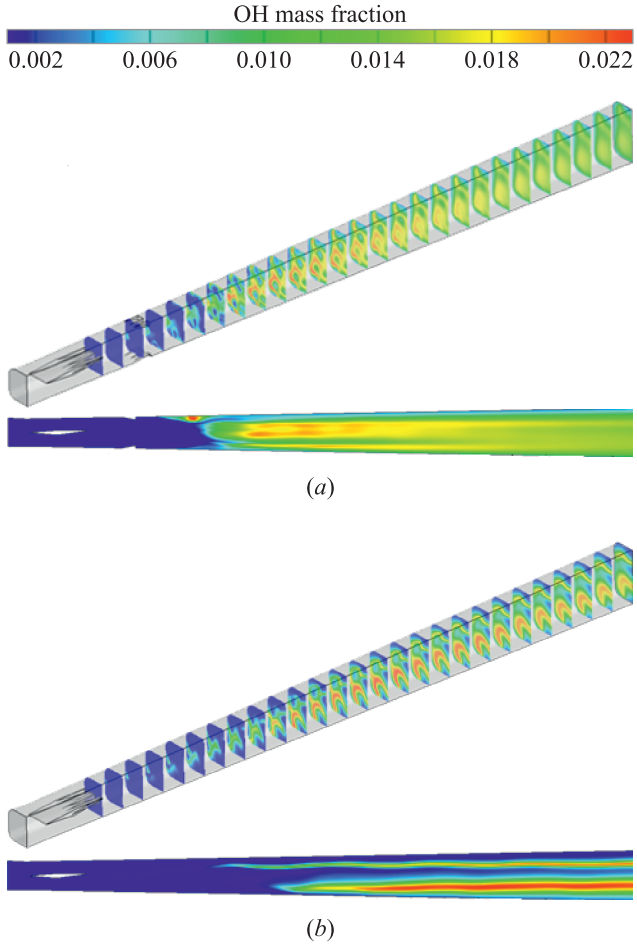

Figure 16 Computed OH mass fraction distribution showing the combustion delay between the single- and the two-staged configurations ($\phi_{\text{tot}} = 0.85$). The 3D model represents half of the combustor. The two-dimensional plot shows a cut at the symmetry plane: (*a*) $\phi_1 = 0.30$ and $\phi_2 = 0.55$; and (*b*) $\phi = 0.85$.

considerably from one configuration to another. For the case using central and wall-ramp injection (see Fig. 15*a*), the field of high temperature due to the combustion covers the whole cross section after 355 mm downstream of the inlet. For the configuration using just central injection (see Fig. 15*b*), the combustion takes place mostly at the central axis of the combustor starting 530 mm downstream. Temperature contours of $T = 300$ K in the wake of the injector show the hydrogen trapped in the vortices produced by the strut injector. Comparing Fig. 15*b* with Fig. 11, it is noticeable that increasing the equivalence ratio, more hydrogen remains trapped in the axial center of rotation of the vortices and a longer distance is required to transport it to the surrounding flow. The distribution of OH mass fraction is plotted in Fig. 16. Combustion is improved using the two-staged combustor configuration. For the same amount of injected hydrogen, the location at which combustion starts is located approximately 150 mm further upstream. However, for all cases, a lifted flame was observed even for $\phi_{\text{tot}} = 0.85$.

4.2 Mixing Efficiency

With the single-stage injection, hydrogen is transported and mixed by the vortices as they travel downstream in the core flow. In the near field of the injection ports, hydrogen is mixed faster due to the strong intensity of the vortices. As the vortices travel downstream, they become weak and some amount of hydrogen still remains unmixed in their axis of rotation. This can be seen in Fig. 17 where the mixing efficiency along the combustor length is plotted. To evaluate the mixing efficiency along the combustor flowpath, the description of Gerlinger *et al.* [5] is used:

$$\eta_{\text{mix}}(x) = \frac{\int\limits_A \alpha \rho u Y_{\text{H}_2}\, dA}{\int\limits_A \rho u Y_{\text{H}_2}\, dA} = \frac{\int\limits_A \alpha \rho u Y_{\text{H}_2}\, dA}{\dot{m}_{\text{H}_2}(x)}$$

with

$$\alpha = \begin{cases} \dfrac{1}{\phi}\,, & \phi \geq 1\,; \\ 1\,, & \phi < 1 \end{cases}$$

where ρ is the density of the gas; Y_{H_2} is the mass fraction of hydrogen; $\dot{m}_{\text{H}_2}$ is the total mass flux of unburned hydrogen through the channel cross section at the position x; A denotes the cross-section area; u is the velocity component normal to the cross section; and ϕ is the local equivalence ratio. The mixing efficiency η_{mix} is defined as the fraction of hydrogen mass flux that could be

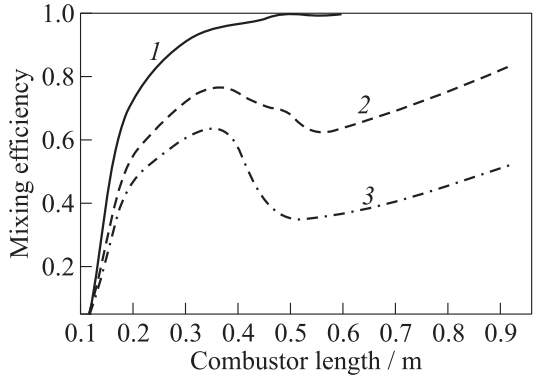

Figure 17 Computed mixing efficiency for the single-staged combustor: *1* — $\phi = 0.30$; *2* — 0.45; and *3* — $\phi = 0.55$

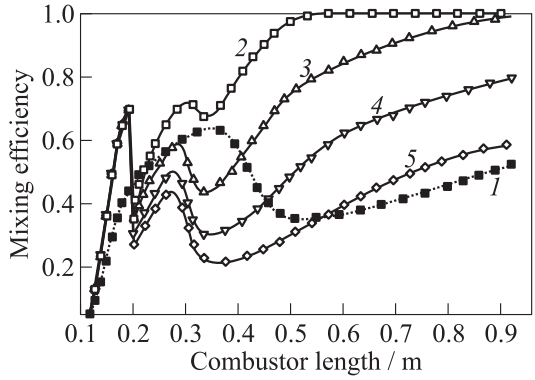

Figure 18 Computed mixing efficiency for the two-staged combustor: *1* — $\phi = 0.55$; *2* — $\phi_1 = 0.30$, $\phi_2 = 0.25$; *3* — $\phi_1 = 0.30$, $\phi_2 = 0.35$; *4* — $\phi_1 = 0.30$, $\phi_2 = 0.45$; and *5* — $\phi_1 = 0.30$, $\phi_2 = 0.55$

burned (at given state of mixing, in case of infinitely fast chemistry) in relation to the total hydrogen mass flux. Hence, $0 \leq \eta_{\text{mix}} \leq 1$, where $\eta_{\text{mix}} = 1$ indicates a perfect mixing and $\eta_{\text{mix}} = 0$ represents complete separation of fuel and oxidizer. Figure 18 shows the computed mixing efficiency for the two-staged injection.

The mixing efficiency is increased using the second injection with the same equivalence ratio. A rapid increase in mixing occurs in the near field of the injection ports where the induced vortices transport and mix the hydrogen to match the available oxygen in the flow. At the wall-ramp injectors, more hydrogen is added and the curve drops but rapidly rises again. Some distance downstream the intensity of the vortices diminished, resulting in a decreased turbulent mix-

ing. At this point, a large amount of hydrogen is already diffused into the flow, then combustion takes place but still some hydrogen remains unmixed. As the combustion starts and moves downstream, the remaining hydrogen is getting mixed and burns, raising again the curve. The mixing process in the combustor is driven by the vorticity induced by the strut injector. Thus, adding more fuel and keeping the same intensity of the vortices is more difficult to diffuse the hydrogen into the flow, and a larger axial length is required for the mixing process. The vorticity induced by the central injector is a geometrical property of the strut [5], sharper geometry could increase the streamwise vorticity and, consequently, the turbulent mixing but, on the other hand, could lead to high pressure losses and, for small combustors, to a blockage. The numerical results show that a combination of central injection together with wall-ramp injection provides better mixing capabilities.

4.3 Influence of Wall Temperature

To investigate the influence of wall temperature on the flow structure inside the combustor, three different wall temperatures were investigated: $T_{\text{wall}} = 300$, 600, and 900 K. The combustion process provides large temperature gradients along the combustor. However, in this set of numerical simulations, three wall temperatures for all surfaces (walls and injector) were selected. The variation of the temperature at the wall shows to have an effect on the peak combustion pressure, length, and location of the shock train. Similar influences were observed by Vyas *et al.* [19]. Figure 19*a* shows the surface pressure distribution at the top wall for $T_{\text{wall}} = 300$, 600, and 900 K with a constant equivalence ratio of $\phi = 0.55$. The results show that the highest pressure peak corresponds to the lowest wall temperature $T_{\text{wall}} = 300$ K and is located in the combustion zone 560 mm downstream of the inlet of the combustor. The first shock caused by the geometrical blockage of the central injector remains unaltered; further downstream, the pressure oscillations become more evident. Before combustion starts ($x < 420$ mm), the pressure peaks are higher for $T_{\text{wall}} = 900$ K, some distance downstream, where the combustion takes place ($x > 420$ mm), the highest pressure peaks are recorded at the "cold wall" temperature $T_{\text{wall}} = 300$ K. After the highest pressure peak, located 560 mm downstream, the difference of the shock train amplitude is more evident between $T_{\text{wall}} = 300$ and 900 K. For $T_{\text{wall}} = 300$ K, the temperature rise due to the combustion begins approximately 490 mm downstream rather than 405 mm for $T_{\text{wall}} = 900$ K. The first signs of OH species appear approximately at the same location where the increase in temperature is registered. For $T_{\text{wall}} = 300$ K, a higher interaction between the shock and the boundary layer is observed due to the large temperature gradient between the wall and the core flow. However, temperatures as low as 300 K are unrealistic in hypersonic flight. No significant difference in axial location of the shock train for $T_{\text{wall}} = 600$ and 900 K was identified. Increasing the wall

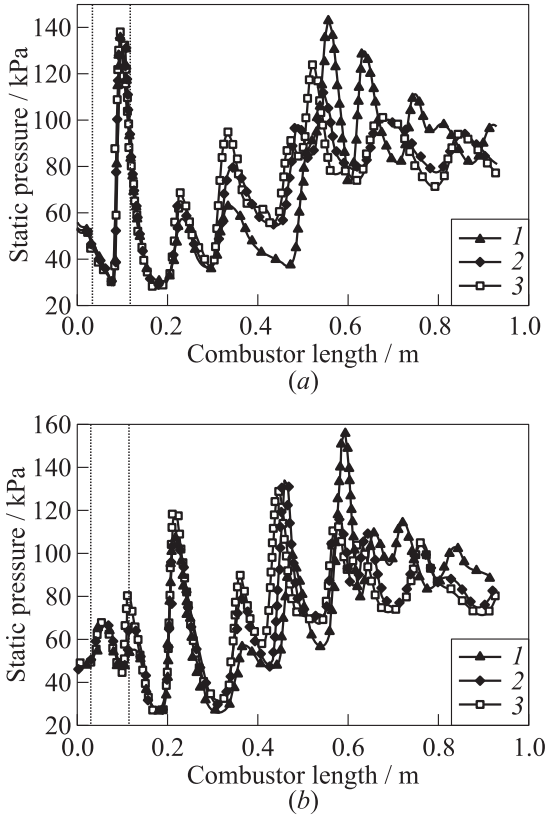

Figure 19 Computed surface pressure distribution at the top (a) and bottom (b) walls for different wall temperatures for $\phi = 0.55$: *1* — $T_{\text{wall}} = 300$ K; *2* — 600; and *3* — $T_{\text{wall}} = 900$ K

temperature results in an upstream displacement of the shock train. Higher wall temperatures enhance the combustion but lead to a complex problems in cooling and structural materials.

Figure 19b shows the surface pressure distribution at the bottom wall. Here, one can observe the asymmetry of the flow due to the high incoming Mach number and the nonuniform flow field.

5 CONCLUDING REMARKS

Numerical simulations of a hydrogen-fueled scramjet combustor with single- and two-staged injection were presented. The two-staged injection configura-

tion showed a better performance in comparison to the single-stage injection. The two-staged injection gives the possibility to increase the amount of injected hydrogen and, thus, to enhance combustion. The turbulent mixing was also improved. For all simulations, a lifted flame was observed. However, the combustion zone starts 150 mm further upstream for the two-staged combustor than for the single-stage. Maximum equivalence ratio of $\phi = 0.85$ was investigated and no thermal choking was observed. Using two-staged injection can reduce the length of the combustor, thus reducing drag and pressure losses. The shock train structures and the surface pressure distributions showed an asymmetry flow along the combustor even for the fuel-off case. This asymmetry in the flow field is caused by the high incoming Mach number and the nonuniform flow profile at the inlet of the combustor. For the single-stage configuration, no separation regions were observed, while for the second-staged injection, small subsonic regions at the top and bottom walls in front of the wall-ramp injectors were visible. These subsonic regions are generated by the injector geometry. The axial location of the subsonic regions was affected by the amount of injected hydrogen while the size of the region was apparently unaffected. The variation of the wall temperature showed an influence on the combustion pressure rise and on the length and position of the shock train. For low temperatures $T_{\text{wall}} = 300$ K, a higher interaction between the shock and the boundary layer was observed. The large temperature gradients between the wall and the flow cause a variation in location of the shock train.

ACKNOWLEDGMENTS

This work was performed within the Research Training Group "Aero Thermodynamic Design of a Scramjet Propulsion System for Future Space Transport Vehicles" (GRK 1095). The first author would like to thank the National Council of Sciences and Technology of Mexico CONACYT for their support. The second author would like to thank the German Research Foundation (Deutsche Forschungsgemeinschaft) for the financial support of the work.

REFERENCES

1. Weigand, B., and U. Gaisbauer. 2009. An overview on the structure and work of the DFG research training group GRK 1095: "Aero-thermodynamic design of a scramjet propulsion system." *16th AIAA/DLR/DGLR Space Planes and Hypersonic Systems and Technologies Conference (International).*
2. Gaisbauer, U., and B. Weigand. 2010. Structure and results of the Research Training Group GRK 1095/2: "Aerothermodynamic design of a scramjet propulsion system:" An overview of the second working phase. *Conference (International) on Methods of Aerophysical Research, ICMAR 2010.*

3. Heiser, W., and D. Pratt. 1994. Hypersonic airbreathing propulsion. AIAA education ser. Washington, DC.
4. Gerlinger, P., P. Kasal, J. Boltz, and D. Brüggemann. 1998. Numerical investigation of the hydrogen strut injections into supersonic air flows. *34th AIAA/ASME/SAE/ASEE Joint Propulsion Conference and Exhibit*.
5. Gerlinger, P., P. Stoll, M. Kindler, F. Schneider, and M. Aigner. 2007. Numerical investigation of mixing and combustion enhancement in supersonic combustors by strut induced streamwise vorticity. *Aerospace Science and Technology*. Elsevier.
6. Scheuermann, T., J. Chun, and J. von Wolfersdorf. 2008. Experimental investigations of scramjet combustor characteristics. *15th AIAA Space Planes and Hypersonic Systems and Technologies Conference (International)*.
7. Vellaramkalayil, J., T. Scheuermann, and J. von Wolfersdorf. 2009. Numerical and experimental investigation of a two-staged supersonic combustion chamber. *16th AIAA/DLR/DGLR Space Planes and Hypersonic Systems and Technologies Conference (International)*.
8. Nguyen, T. 2011. Numerical investigations of relaminarization in scramjet flows. Ph.D. Dissertation. Aachen, Germany: RWTH Aachen University.
9. Metacomp Technologies Inc. CFD++ User Manual. Version 10.1.
10. Banica, M. C., J. Chun, T. Scheuermann, B. Weigand, and J. von Wolfersdorf. 2009. Numerical investigation of the performance of a supersonic combustion chamber and comparison with experiments. *6th European Symposium on Aerothermodynamics for Space Vehicles*. Versailles, France.
11. Gerlinger, P., H. Möbus, and D. Brüggemann. 2001. An implicit multigrid method for turbulent combustion. *J. Comput. Phys.* 167:247–76.
12. Mack, A., and J. Steelant. 2008. Scaling and optimization of the injection, mixing and combustion for a generic scramjet combustion chamber. LAPCAT Project. ESA-ESTEC.
13. Berglund, M., E. Fedina, C. Fureby, J. Tegnér, and V. Sabelnikov. 2010. Finite rate chemistry large-eddy simulations of self-ignition in a supersonic combustion ramjet. *AIAA J.* 48(3):540–50.
14. Carroll, B., and J. Dutton. 1990. Characteristics of a multiple shock wave / turbulent boundary-layer interaction in rectangular ducts. *J. Propul.* 6(2):186–93.
15. Smart, M., N. Hass, and A. Paul. 2006. Flight data analysis of the HyShot 2 scramjet flight experiment. *AIAA J.* 44(10):2366–75.
16. Hannemann, K., S. Karl, J. Martinez, and J. Steelant. 2010. Methodology of a combined ground based testing and numerical modeling analysis of supersonic combustion flow paths. *Shock Waves J.* 20(1):353–66.
17. Fureby, C., M. Chapuis, E. Fedina, and S. Karl. 2010. CFD analysis of the HyShot II scramjet combustor. *Proc. Combust. Inst.*
18. Wang, C., K. Zhang, C. Zhou, B. Sun, and X. Cao. 2007. Experimental study of shock train in a scramjet isolator. *ISABE 2007*.
19. Vyas, M., W. Engblom, N. Georgiadis, C. Trefny, and V. Bhagwandin. 2010. Numerical simulation of vitiation effects on a hydrogen-fueled dual-mode scramjet. *48th Aerospace Sciences Meeting*. AIAA.